Original Research

Dependence of Vessel Area Accuracy and Precision As a Function of MR Imaging Parameters and Boundary Detection Algorithm

Jing Jiang, MS,[1–3] E. Mark Haacke, PhD,[1,2*] and Ming Dong, PhD[3]

Purpose: To determine the appropriate image acquisition parameters for an accurate measurement of vessel cross-sectional area from MR angiography (MRA) images.

Materials and Methods: A series of images with different vessel cross-sectional areas, resolutions, and signal-to-noise ratios (SNRs) were simulated and validated experimentally. Dynamic programming (DP) was employed to determine the accuracy and precision of the vessel cross-sectional area as a function of vessel size, sampling matrix, acquisition time, and postprocessing parameters such as zooming and bias correction.

Results: We show that there is an optimal value of λ (the ratio of vessel diameter to resolution) for a given intrinsic SNR that yields the most accurate and precise area measurement. Specifically, when the SNR is $\geq$10:1, this value of λ is 8 and yields a cross-sectional area error of $<$5% with a zoom factor of $\geq$2.

Conclusion: The predicted ideal result of $\lambda = 8$ is within reach with current technology to image vessels such as the carotid artery or aorta. It is possible to determine the ideal resolution that minimizes errors in the measurement of the vessel cross-sectional area for a given SNR, processing algorithm, and vessel of interest.

Key Words: vessel cross section; dynamic programming; high-resolution MR angiography; zero-filled interpolation; quantification of other osclerosis
J. Magn. Reson. Imaging 2007;25:1226–1234.

ATHEROSCLEROSIS, A DEGENERATIVE DISEASE of the arteries, is a leading cause of death and impairment in the United States. In 1994 it was estimated that 64,400,000 Americans were affected by one or more types of cardiovascular disease (1). Magnetic resonance imaging (MRI) is a powerful means of noninvasively imaging the blood vessels in the human body. It can be used not only to visualize the vessel but also to measure its cross-sectional area; however, numerous inaccuracies can arise in determining the cross-sectional area, even when flow-related artifacts are absent (2). These are caused by intraluminal saturation effects, poor resolution and signal-to-noise ratio (SNR) (3,4). The North American Symptomatic Cartoid Endarterectomy Trial (NASCET) study of carotid stenosis (5) indicated that it is best for the patient to undergo surgery if the stenosis is greater than 70%. A critical question for investigators is, if we wish to use MRI data to make this determination, how accurately must we measure the vessel cross-sectional area? In practice, this error is required by the physician to be $\leq$5%. Technically, we need to determine what resolution and SNR are good enough to obtain acceptable results. In this paper we consider linking the quantitative evaluation of cross-sectional area with the image acquisition parameters. This important step has the potential to answer a related question: If we know the accuracy with which we need to evaluate the vessel cross section, how should the MRI data be collected?

In practice, a radiologist will determine the degree of stenosis on a 3D workstation with zooming and interpolation capabilities. The minimum stenotic diameter is compared with the diameter of a nearby normal vessel. This is done by using multiplanar reformatting of the source images to create an image of the cross section of the vessel perpendicular to the direction vector of the vessel. An automated segmentation algorithm is often used to reproducibly measure the cross-sectional area. A number of authors have investigated the role of spatial resolution and SNR in this important segmentation problem (6–13). The algorithms used include an active contour of local regions of interest (ROIs) (7,8), thresholding (12), full width at half maximum (FWHM) to obtain the vessel diameter (9), automatic wave propagation to extract the centerline (6), and edge compensation methods to compensate for the loss of edge details in the maximum intensity projection (MIP) image (10,11,13). A similar approach to the one we propose here has been taken by several groups (14–17) to look at vessel wall measurements. These authors examined the roles of resolution and SNR, but not the roles of the

[1]Radiology Department, Wayne State University, Detroit, Michigan, USA.
[2]MRI Institute for Biomedical Research, Detroit, Michigan, USA.
[3]Computer Science, Wayne State University, Detroit, Michigan, USA.
*Address reprint requests to: E.M.H., 440 E. Ferry Street, Detroit, MI 48202. E-mail: Nmrimaging@aol.com
Received February 3, 2006; Accepted December 21, 2006.
DOI 10.1002/jmri.20918
Published online in Wiley InterScience (www.interscience.wiley.com).

processing methods and scalability, or the effects of zooming the images.

In this work, we present a complete analysis of these issues for a given vessel segmentation method in order to design an MR experiment to obtain the best result for cross-sectional area measurements.

MATERIALS AND METHODS

The approach we take is to simulate MR images with varying SNR and resolution, which are critical parameters for evaluating MRA image quality (18). A specific dynamic programming (DP) method is then used to evaluate just how well the cross-sectional area of a vessel can be found for a given SNR and resolution. We also consider the effect of zooming prior to data analysis. Once good accuracy and precision have been obtained, we can search for an optimal solution in terms of resolution and SNR to collect the data (19). The theoretical predictions are then compared with experimental MR data collected from a tube filled with water.

MR Vessel Model

We want to simulate the cross-sectional view of a vessel by means of a perfect circle against a background of no signal or noise. First we create a base image with a 4096×4096 matrix, which is given an intensity of 500 inside the circle and 0 outside. Specifically, a 4096×4096 Fourier transform is performed to mimic an analytic transform similar to that which would be collected in a real MR system. In the frequency domain, we keep only matrices with the following pre-selected sizes: 128×128, 256×256, 512×512, or 1024×1024. We then transform the data back to the image domain, which creates an image that has the usual Gibbs ringing effect.

Segmentation Using DP

At this stage we use DP to find the boundary of the object (which in this example is the simulated circle) and calculate the area of this object. For future reference, we will call the simulated circle "circle A." DP requires an initial guess of the object edge, which for our study is selected as a circle ("circle B") with a fixed center point at the center of circle A, and a diameter that is 4 pixels larger than the diameter of circle A. This mimics the step of a radiologist drawing a first guess outside the vessel. An overview of all the steps involved is provided by the flow chart in Fig. 1.

The cross section for the vessel is found using a DP approach. As usual, an objective function is used to combine edge detection with a constraint. The cost function is evaluated on a ray-by-ray basis from a chosen center point of the vessel and followed along this ray toward circle B. It consists of a derivative term and a radius-limiting term to avoid leakage and to cut through any potential vessel bifurcations. Specifically, we propose to identify the points on the boundary by maximizing the following objective function $C(r,m)$:

$$C(r, m) = \frac{G(r,m)}{G_{max}} - \alpha^* \frac{Var(R(r,m))}{R_{range}} \qquad (1)$$

where the gradient and the radius along the m^{th} ray at the r^{th} point are denoted by $G(r,m)$ and $R(r,m)$, respectively. The term G_{max} provides normalization and represents the maximum derivative along the ray, and $\pm R_{range}$ refers to the search range on each ray (usually R_{range} is set to 4 pixels). Here α is a constant larger than zero and represents the relative weighting of the gradient and variance terms. In practice, we have found that α between 0.2 and 3 creates an appropriate balance that leaves enough flexibility for the derivative term to dominate, but allows the radius term to keep the arcs slowly varying and prevent leakage. In the studies described below, we use α equal to 1. The term $Var(R(r,m))$ gives the normalized radius variance for the set of four points that includes the point (r,m) for any r^{th} point on the m^{th} ray and the three previously selected points on the boundary. It is defined as:

$$Var(R(r,m)) = \sqrt{((R(r,m) - Avg(r, m))^2 + \sum_{i=m-3}^{m-1} (R_i - Avg(r,m))^2)} \qquad (2)$$

where R_i is the radius of the selected point of the i^{th} ray on the boundary, and $Avg(r,m)$ is the average over the four radii $R(r,m)$ and R_{m-1}, R_{m-2}, R_{m-3} from the previous three.

Definitions

Our goal is to consider the effects of varying noise levels, vessel diameters, and sampling matrices. In the simulations we used a standard random number generating algorithm in Monte Carlo analysis to generate Gaussian noise. Each time an image is generated, a different seed point is used, and therefore no set of random numbers is the same. The SNR can be described as the signal inside the circle (which is 500 in our simulation) divided by the standard deviation (SD) of the Gaussian noise. The DP method is used to find the cross-sectional area A for each different case. The diameter is varied from 64 to 256 pixels in a 4096×4096 original simulated image, the SNR is varied from 80:1 to 2.5:1, and the sampling matrix size is varied from 128×128 to 1024×1024. Instead of depending on the sampling matrix size or vessel radius separately, we expect that the DP method should depend more on their relative ratio, so we define a scale invariant parameter λ as the ratio of the diameter of the vessel divided by the resolution of the image:

$$\lambda = \frac{D_0}{\Delta x} \qquad (3)$$

where D_0 is the actual vessel diameter, and Δx is the resolution in the image (i.e., λ is the number of pixels across the diameter of the vessel).

In the simulation data we define the resolution in terms of number of pixels as S_o/S_s, where S_s is the size of the sampling matrix and S_o is the size of the original

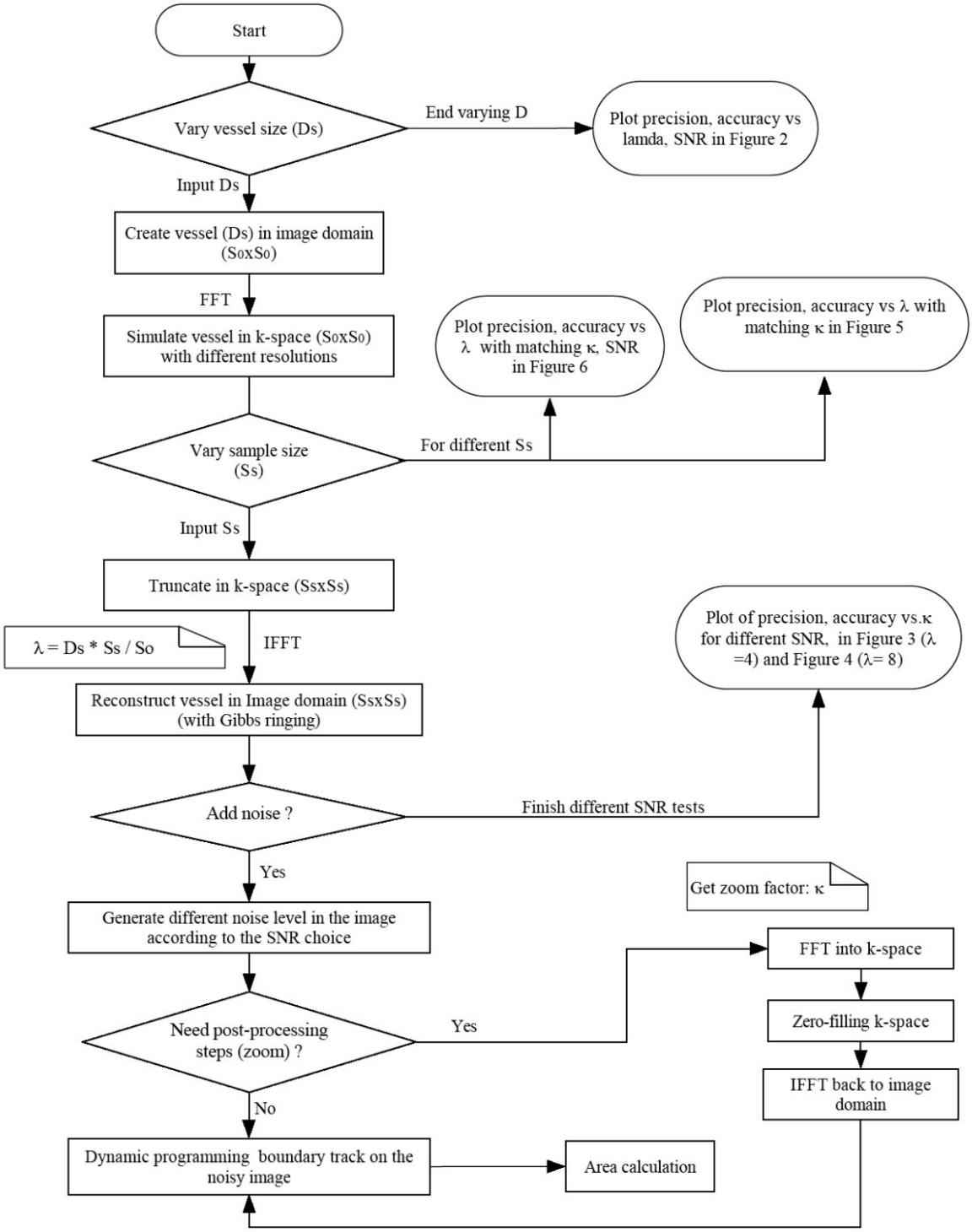

Figure 1. Flow chart of the image simulation, postprocessing techniques, and measurement errors vs. SNR, resolution, and zoom factor.

image (4096 in our case). With this definition, we rewrite λ as

$$\lambda = D_s * \frac{S_s}{S_0} \tag{4}$$

where D_s is the vessel diameter in terms of the number of pixels in the original 4096 image. The range of λ is 4–64 for our experiments and is obtained by varying D_s, the vessel diameter, from 64 to 256 pixels in the 4096 × 4096 original image and varying S_s, the sampling matrix, from 128 × 128 to 1024 × 1024.

For a given set of parameters, including noise levels, vessel radii, and size of sampling matrices, the DP is run 30 times through a Monte Carlo simulation (20). We then obtain the mean and SD (precision) for the

vessel area. The accuracy is obtained by examining the bias of the DP method:

$$bias = \frac{(A_{mean} - A)}{A} - \xi \tag{5}$$

where A_{mean} is the mean of the vessel area from 30 simulations, A is the actual vessel area, and ξ is defined as a system bias. The algorithm used here tends to choose the halfway mark of the blurred profile through the image and therefore tends to overshoot the true diameter by 0.5 pixels. The area size will be $\pi \times (r + 0.5)^2$ instead of $\pi \times r^2$, and $\lambda = 2r$ as we defined in Eq. [3], which leads to a system bias ξ of roughly:

$$\xi = \left\{\frac{[\pi^*(\lambda/2 + 0.5)^2]}{(\pi^*\lambda/2^2)}\right\} - 1 \approx 2^*0.5^* \frac{\lambda/2}{\lambda/2^2} = \frac{2}{\lambda} \tag{6}$$

We use the zero-filling method for image zooming (21) and compare the segmentation results after interpolating the images so that the product of the interpolation factor (the zoom factor κ) and the vessel diameter to pixel dimension ratio (λ) will be a constant. This means that after interpolation the vessel diameters will appear to be the same even though they were actually collected with different resolutions. In other words, the vessels are normalized so that β is a constant, where β is defined by

$$\beta = \kappa^*\lambda \tag{7}$$

To touch base with a real-world situation, when comparing different matrix sizes we take into account the fact that SNR changes. We also consider the case in which the total scan time is constant. (The noise increases linearly with the size of the acquisition matrix for 2D imaging when matrix sizes are simultaneously changed in both directions and total bandwidth is held constant (22)).

Simulations

The results for SD and bias are best displayed as a function of the scale parameter λ. For the same λ we run the DP on different combinations of resolution and vessel diameter, which allows us to test the assumption that the data depend on λ and not separately on the resolution or vessel diameter, as shown in Fig. 2. There is no zoom in this simulation step. (Each combination of the parameter sets of resolution and vessel diameter is tested for five SNR values, and each SNR has 30 Monte Carlo simulation steps. A total of 1500 images are evaluated in this step.) The case for $\lambda = 4$ is considered first.

We repeat the tests after zooming the same image by factors of 2, 4, 8, and 16 for an object of diameter 64 initial pixels out of 4096 in the sampling matrix size of 256×256, (which is $\lambda = 4$ by our definition). Results for precision and accuracy are shown in Fig. 3 (a total of 900 images are evaluated in this step). A similar simulation comparing the zoom factors effects for $\lambda = 8$ is shown in Fig. 4 for precision and accuracy.

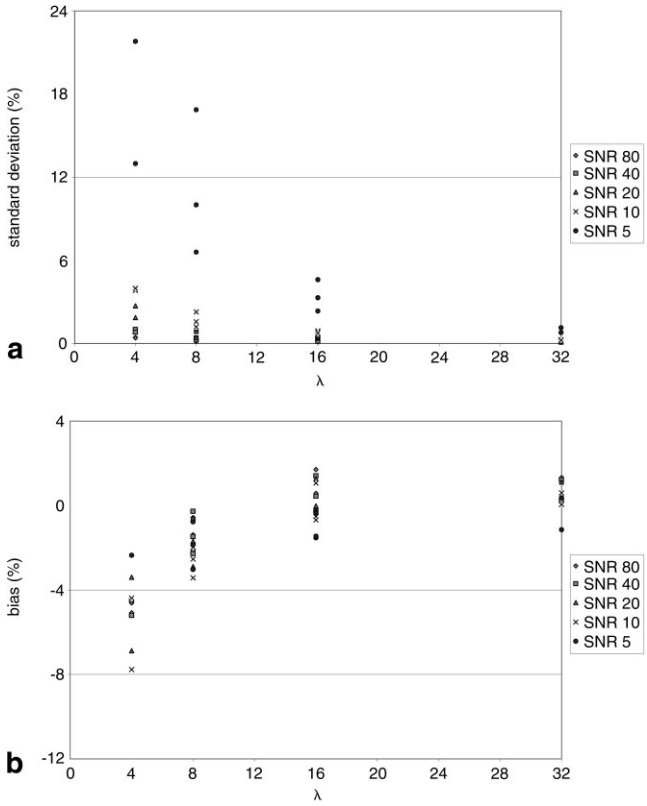

Figure 2. a: SD of vessel area in percent vs. λ for different SNR levels without zooming. **b:** Bias of vessel area in percent vs. λ for different SNR levels without zooming.

We also evaluated the normalized cross-sectional area measurement accuracy and precision for a vessel of diameter 64 initial points (D_s) for a set of three sampling matrices (256×256, 512×512, and 1024×1024). We kept β fixed at 16. In Fig. 5a (for precision) and 5b (for bias), the image from the sampling matrix 256×256 ($\lambda = 4$) has been zoomed by 4, the image of the 512×512 matrix ($\lambda = 8$) has been zoomed by 2, and the image of the 1024×1024 matrix ($\lambda = 16$) has not been zoomed. However, increasing the sampling matrix will result in higher noise levels, and we take this into account. The starting SNR refers to that measured in the sampling matrix (256×256). The SNR is decreased to one-half when sampled to 512×512, and to one-quarter when sampled to 1024×1024. Putting all this together, we wish to determine the best resolution to use for a given SNR (a total of 360 images are evaluated in this step).

We further increased β to 128 and repeated similar simulation steps for a vessel of diameter 64 initial points under the same given SNR (Fig. 6). The image of $\lambda = 4$ (from the sampling matrix 256×256) has been zoomed by 32, the image of $\lambda = 8$ (from the 512×512 matrix has been zoomed by 16), and the image of $\lambda = 16$ (from the 1024×1024 matrix) has been zoomed by 8 (a total of 360 images are evaluated in this step). The starting SNR is measured in the sampling matrix (256×256) similarly to the approach used in Fig. 5.

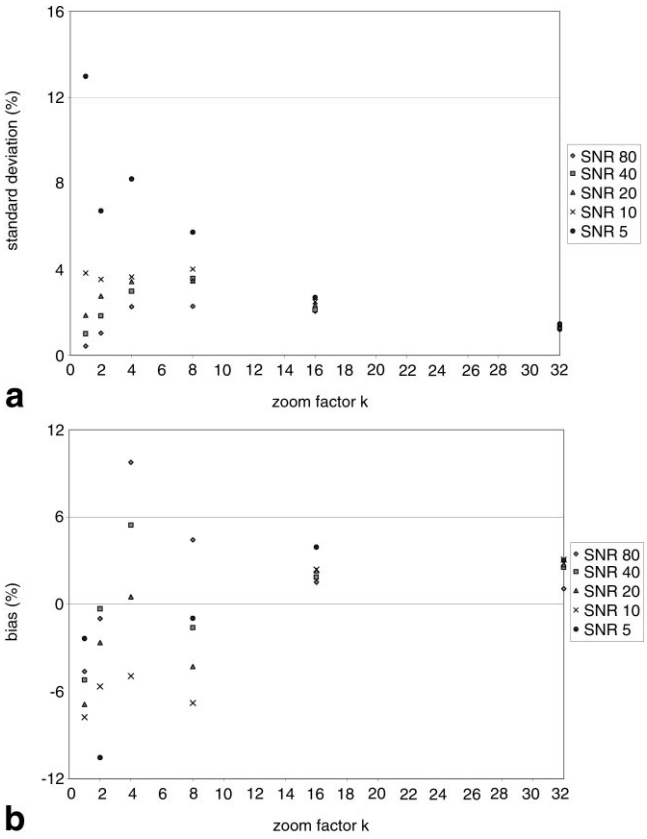

Figure 3. a: SD of vessel area in percent vs. zoom factor for different SNR levels and $\lambda = 4$. **b:** Bias of vessel area in percent vs. zoom factor for different SNR levels and $\lambda = 4$.

In Vitro MRA Experiment

To test the results from the simulations, we ran an experiment on a 4.7T Bruker Bio SPEC using a U-tube phantom with an internal diameter of 4 mm and a length of 8 cm. The cross-sectional image of the phantom is shown in Fig. 7a. The imaging parameters included FOV = 3.2 cm × 3.2 cm, TR = 62 msec, TE = 8.87 msec, and FA = 10°. We varied the resolution from 125μm × 125μm to 250μm × 250μm, 0.5 mm × 0.5 mm, and finally 1 mm × 1 mm. From the definition of λ in Eq. [4], we know that $\lambda = 4$ in the 1 mm × 1 mm image, and 32 in the 125 μm × 125 μm image. We also varied the SNR by changing the slice thickness (TH) and performing multiple acquisitions (Nacq), and then averaging the data as follows: TH = 1 mm, Nacq = 1; TH = 2 mm, Nacq = 1; TH = 1 mm, Nacq = 2; and TH = 2 mm, Nacq = 2 (a total of 16 sequences were run).

The starting SNR is 24, as measured from the signal mean inside the phantom and the noise mean outside the phantom from an image with a resolution of 1 mm × 1 mm, TH = 1 mm and Nacq = 1. The SNR is decreased to 12 for a resolution of 0.5 mm × 0.5 mm with the same TH and Nacq. The SNR decreases further to 6 for a resolution of 250μm × 250μm, and to 3 for resolution 125μm × 125μm with the same TH and Nacq. The highest starting SNR, which is 68, is achieved with a resolution of 1 mm × 1 mm, TH = 2 mm, and Nacq = 2. The second-highest starting SNR is 48, which is represented in the image with a resolution of 1 mm × 1 mm, TH = 2 and Nacq = 1. The starting SNR is 34 in the image with resolution 1 mm × 1 mm, TH = 1 mm, and Nacq = 2. As discussed above, the lowest starting SNR is achieved with a resolution of 1 mm × 1 mm, TH = 1 mm, and Nacq = 1.

For one starting SNR we evaluated the normalized cross-sectional area measurement accuracy and precision for the phantom of 4-mm diameter. We kept β constant at 32. We also took into account that the SNR drops by half as λ doubles. The result of bias vs. λ for different starting SNR levels is shown in Fig. 7b.

RESULTS

In Fig. 2 the plots of the different resolutions, vessel diameters, and SNR levels without zooming are grouped by λ. These graphs show that precision and accuracy depend on λ and not independently on resolution and vessel diameter. We also see that the SD of the cross-sectional area reduces by roughly $1/\lambda$ independent of the noise level. The results for the bias depend quite strongly on λ. In general, as expected, the bias and the SD have a larger range of oscillation as noise increases, and converge when noise decreases (Fig. 2). The partial-volume effect occurs in the measurement because all of the pixels that contain the boundary will be counted no matter how small a voxel fraction is included by the boundary (23).

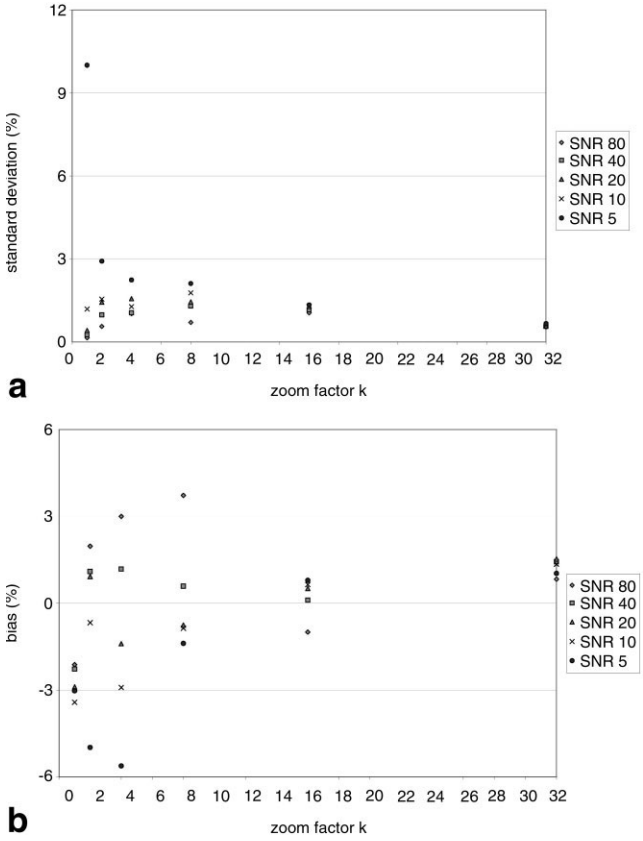

Figure 4. a: SD of vessel area in percent vs. zoom factor for different SNR levels and $\lambda = 8$. **b:** Bias of vessel area in percent vs. zoom factor for different SNR levels and $\lambda = 8$.

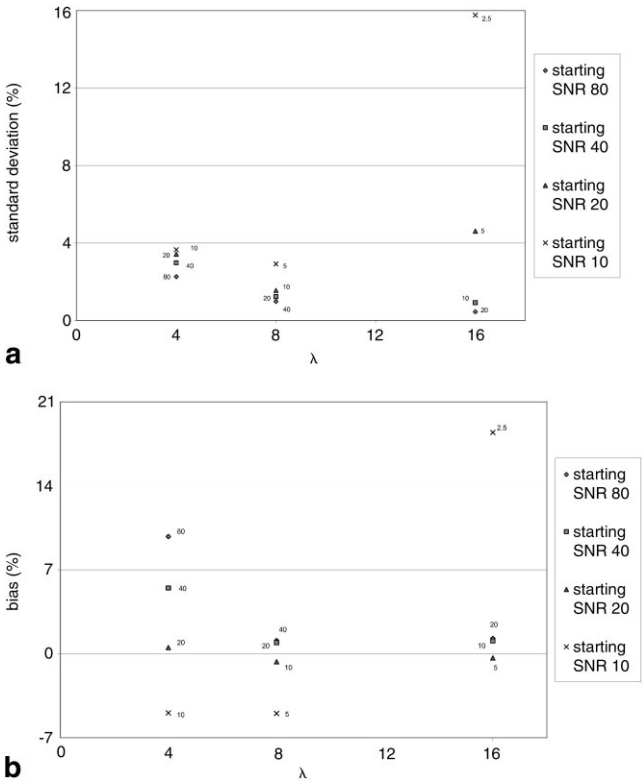

Figure 5. a: SD of vessel area in percent vs. λ for a vessel of diameter 64 at four different starting SNR levels with constant β = 16. **b:** Bias in percent vs. λ for a vessel of diameter 64 at four different starting SNR levels with constant β = 16.

Postprocessing, zero-filling zooming plays a significant role in reducing error (both bias and SD). When the zoom factor, κ, increases from 1 to 32, the precision decreases from 13% to 1.5% with SNR = 5:1 for λ = 4 (Fig. 3). For λ = 8, as κ increases from 1 to 32, precision decreases from >10% to <1% for the same SNR = 5:1. The bias error shifts from negative to positive, with the absolute value decreasing to zero as κ increases (Figs. 3b and 4b). The SNR also affects the accuracy and precision. In general, the higher the SNR the better the accuracy and precision will be. However, the SNR plays a more significant role for smaller zoom factors than for larger zoom factors. When the zoom factor κ is ≥16, the difference in precision due to the different SNRs is <1% and the difference in accuracy is <3% (Figs. 3 and 4).

In the realistic examples, the precision and accuracy are not guaranteed to improve when the resolution gets better, especially for a low starting SNR because the noise dominates as resolution increases. The λ = 8 case (sampling matrix = 512 × 512) is the best choice for all four starting SNR values (Fig. 5) for β = 16, which yields a precision of >3% and a bias of <5%. For SNR ≥ 10:1, the λ = 8 case generates an error (including precision and accuracy) of <3%.

If we increase the zoom factor κ by a factor of 8, β will be increased to 128. Using the same combinations as in Fig. 5, we find that the λ = 8 case (sampling matrix = 512 × 512) is the still best choice (Fig. 6) to obtain the smallest error. The precision and accuracy both drop to <1.5% for λ = 8. We can see that λ = 4 also yields a good performance, with an accuracy of <4% and precision of <2%. To save precious sampling time, λ = 4 is an optimal choice.

We also consider three vessels of different diameters: the aorta, the carotid, and the coronary artery (see Table 1). We simulated a 75% stenosis by cutting λ in half from the healthy portion of the vessel to the diseased portion. The entries in Table 1 are extracted from Fig. 5. We did not go to a higher zoom because the result was good enough to satisfy the 5% error requirement. The results (i.e., the accuracy and precision of the stenosis measurement relative to the healthy portion) indicate that a choice of λ_h (healthy vessel) = 8 to λ_d (diseased vessel) = 4 or higher value of λ_h but with $\lambda_h/\lambda_d \leq 2$ will satisfy the requirement that both precision and bias must be less than 5%.

Let us consider the implications of this for three vessel types (aorta, carotid, and coronary artery) with 75% stenosis. In Table 1 we consider a specific resolution that keeps the errors in each case on the order of 5% for reasonable imaging parameters. We simulate a 75% stenosis by cutting λ in half from the healthy portion of the vessel to the diseased portion. The entries in this table are extracted from Fig. 5. The accuracy of the stenosis measurement ($\delta_{stenosis}$) relative to the healthy portion of the vessel is defined by the following function:

$$\delta_{stenosis} = \frac{A_2(1+\delta_2)}{A_1(1+\delta_1)} - \frac{A_2}{A_1} \tag{8}$$

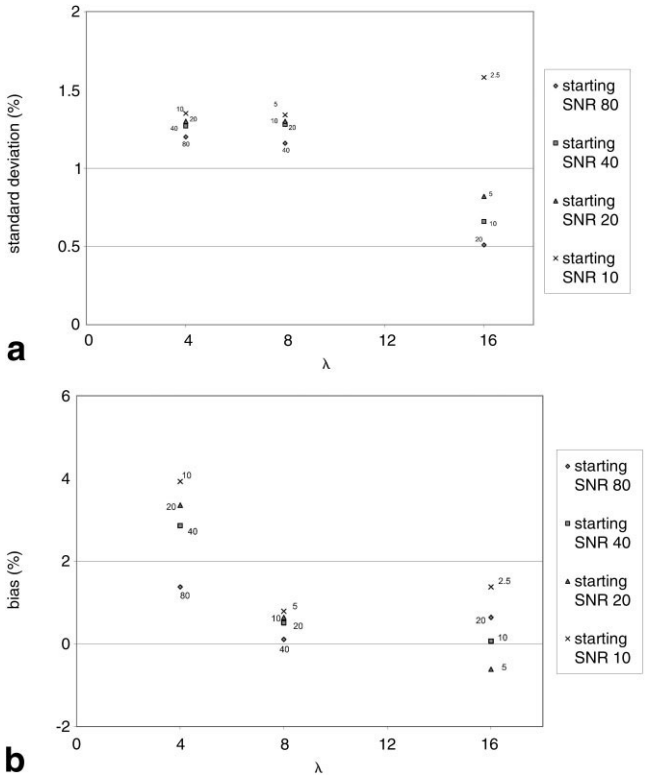

Figure 6. a: SD of vessel area in percent vs. λ for a vessel of diameter 64 at four different starting SNR levels with constant β = 128. **b:** Bias in percent vs. λ for a vessel of diameter 64 at four different starting SNR levels with constant β = 128.

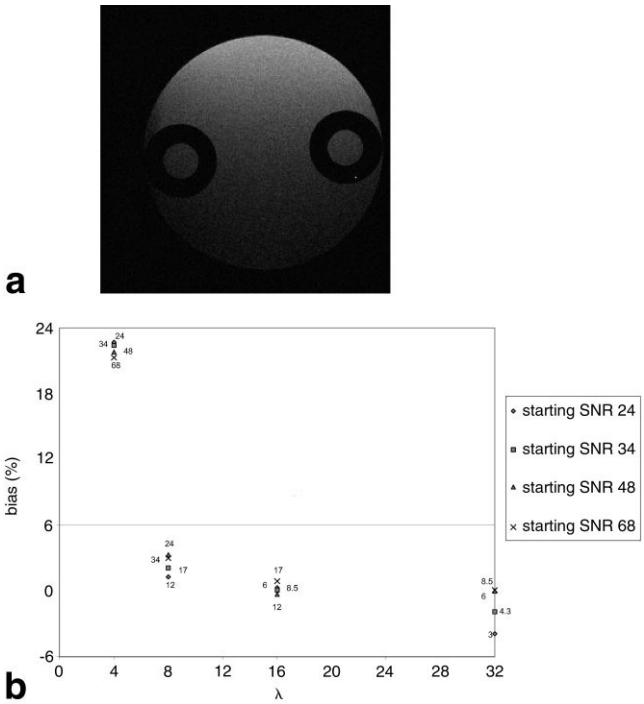

Figure 7. a: Phantom of 4-mm diameter (FOV = 3.2 × 3.2, TR = 62ms, TE = 8.87 s, FA = 10°, resolution = 250 μm × 250 μm). **b:** Bias in percent vs. λ for a phantom of 4-mm diameter at three different starting SNR levels with constant β = 32.

where A_1 and A_2 are the areas of the healthy and diseased regions, respectively; A_2/A_1 equals 25%; and δ_1 and δ_2 represent their respective biases. The precision of the stenosis measurement ($\sigma_{stenosis}$) relative to the healthy portion is defined by the following function of the precision of the healthy (σ_1) and diseased (σ_2) regions:

$$\sigma_{stenosis} = \sqrt{((\sigma_1)^2 + (\sigma_2)^2)} * \frac{A_2}{A_1} \quad (9)$$

The values for $\delta_{stenosis}$ and $\sigma_{stenosis}$ are presented in Table 1. The resulting errors and total error are found to be less than 5%. These results indicate that a choice of λ = 8 to λ = 4 or higher meets the requirements set forth in this study.

DISCUSSION

The results clearly show that the optimum choice of imaging parameters for quantifying vessel cross sections depends predominantly on λ and SNR, since as these two parameters increase, the accuracy and precision also increase. Zooming can also help. For small λ with poor SNR, zooming plays a significant role in improving the measurement accuracy, as shown in Figs. 3 and 4. Overall, the desired performance (i.e., absolute value of bias + SD = <5%) was achieved with λ = 8, SNR ≥ 10, and κ ≥ 2 (Fig. 4), or λ = 4, SNR ≥ 5, κ = ≥16 (Fig. 3). Figures 5 and 6 further support the conclusion that there is one optimum value of λ for SNR ≥ 10: λ = 8. Given the increases in time that are required for higher resolution, and the incremental improvement in accuracy and precision, there is little need to pursue higher λ.

The SD (Figs. 3a and 4a) and bias (Figs. 3b and 4b) decrease as the zoom factor κ increases. This is because the partial-volume effect can be overcome after the process of zero-filling interpolation is completed (21). We can safely give the conclusion the higher the zoom factor, the smaller the SD and bias. Using a larger zoom factor κ will generate better precision and accuracy, which strongly supports the role of interpolation in area measurement and can in part compensate for smaller λ. Here β, the product of λ and κ, is the key parameter that determines the precision and accuracy. For smaller λ, a larger κ is needed to achieve the same accuracy and precision. For example, the precision decreases below 3% when κ = 16, while the bias decreases below 4% for λ = 4 (Fig. 3). For λ = 8, κ = 8, the accuracy and precision reduce below 4% and 3%, respectively (Fig. 4).

Table 1
Example of Stenosis Measurement Error for the Aorta, Carotid Artery, and Coronary Artery With 75% Stenosis

	Aorta		Carotid		Coronary	
Diameter	16 mm		8 mm		4 mm	
Resolution	1 mm		1 mm		0.5 mm	
SNR	5:1		10:1		10:1	
Vessel λ	Healthy region (λ = 16)	Diseased region (λ = 8)	Healthy region (λ = 8)	Diseased region (λ = 4)	Healthy region (λ = 8)	Diseased region (λ = 4)
Precision of area measurement	4.6%	2.9%	1.5%	3.7%	1.5%	3.7%
Accuracy of area measurement	–5.0%	–0.4%	–0.7%	–4.9%	–0.7%	–4.9%
$\delta_{stenosis}$	–1.2%		–1.1%		–1.1%	
$\sigma_{stenosis}$	1.4%		1.0%		1.0%	
Stenosis expression 75% + $\delta_{stenosis} \pm \sigma_{stenosis}$	75%–1.2% ± 1.4%		75%–1.1% ± 1.0%		75%–1.1% ± 1.0%	

$\delta_{stenosis}$ = the accuracy of the stenosis measurement relative to the healthy region defined in Eq. [8], $\sigma_{stenosis}$ = the precision relative to the healthy region defined in Eq. [9].

With the current use of contrast agents, the SNR values for the blood may well be larger than what we chose for the examples given above, and hence investigators' ability to estimate stenosis will only improve. It is probably best to go to a resolution of 0.5 mm in narrower regions of the carotids or in the middle coronary vessels to keep the errors under 5%.

The particular algorithm we used in this study may well not be the best available. In fact, by changing the choice of method to determine subtle differences in the edge locations (such as using partial-volume information or choosing specifically FWHM or full width at 30% maximum (12)), one could reduce the bias for low values of λ. Currently our algorithm performs best (total error $< 5\%$) as far as bias is concerned for $\kappa \geq 8$ for $\lambda = 4$, and $\kappa \geq 4$ for $\lambda = 8$. Clearly, the lower value of κ is preferred to save processing time, and the lower value of λ is preferred to achieve the shortest acquisition time.

The results of Figs. 5 and 6 are based on the assumptions that SNR drops as the square root of the voxel size. In fact, the drop can be much faster. For example, if we consider the SNR per unit time, there will be another loss of $\sqrt{2}$ if resolution is doubled. Even worse, as the matrix size increases, the standard sequences used in the industry lead to an increase in bandwidth (to keep the sampling time constant), which creates yet another loss of $\sqrt{2}$ in SNR. Therefore, in the worst-case scenario, SNR drops as the voxel volume. What implications does this have for the best choice of λ? Consider the case in which $\lambda = 4$ and SNR = 40:1. If SNR drops to 10:1 (the SNR of 40:1 for $\lambda = 4$ drops to an SNR of 10:1 for $\lambda = 8$) as λ increases to 8, this point is no longer represented by the triangle but rather by the diamond (which has an SNR of 10:1 in Figs. 5 and 6 for $\lambda = 8$). Interestingly, we conclude that we still would choose $\lambda = 8$ as the ideal solution. The larger value of λ has the advantage of leading to a lower bias. Therefore, if there is enough time to collect images with $\lambda = 8$, this is to be preferred. Carrying this to the next step ($\lambda = 16$) means an SNR of 2.5:1, and the crossing of $\lambda = 16$ now represents the triangle. Clearly, this is not good because the error will increase to more than 15% in both precision and accuracy.

The effects of further modifications to this algorithm may well lead to further improvements in precision. Any new method can also be tested via simulations to create cross-sectional area estimates similar to those shown in Figs. 5 and 6. Although other improvements may be implemented, we expect that the general behavior of the curves will stay the same.

For the U-tube phantom experiment, the bias is less than 3% for $\lambda \geq 8$, validating the results of the simulations shown in Figs. 5 and 6. These experimental data also behave very similarly to those of the simulation results as a function of resolution.

We have shown that zooming helps overcome the digitization error associated with approximating an analog object by a digital image, especially for small λ. This error creates a bias even when there is no noise. The higher zoom factor, the lower the error. Using a zoom factor of at least 2 is worth the effort not only for bias improvement but also for better vessel detection and vessel tracking (21,24,25).

The approach we present here is not limited to imaging vessels. Figures 5 and 6 can be used to estimate the accuracy of any cross-sectional measurement in other structures, such as the caudate nucleus (3). For example, as the cross-sectional areas change throughout the volume, the error in each can be calculated, and hence the total error in the volume estimate can be calculated.

At 1.5T and higher, the contrast-to-noise ratio (CNR) in conventional MRA scans can well exceed 20:1 for the scenarios described in this paper. The use of contrast agents (10,12) can further increase this number. Also, resolution can be improved easily from 1 mm to 0.5 mm and even 0.25 mm with the use of new fast parallel imaging techniques (26).

Therefore, it is well within our grasp to collect images with high SNR and resolution to enable the next generation of clinical MRA data to be collected with $\lambda = 8$ (even in the proximal coronary arteries) so that the error in measuring a 75% stenosis will be below 5% and close to 3% for accuracy (in Fig. 6b, for $\lambda = 8$ and 16, all errors are $<3\%$; for $\lambda = 4$, SNR = $\geq$40:1, all errors are $<3\%$) and 2% for precision (in Fig. 6a, all errors are $<2\%$).

In conclusion, the results of our simulations and phantom experiment indicate that there is an optimal choice of λ and zoom factor κ to obtain the best estimate of the cross-sectional area for a given SNR. Considering the opposing roles of sampling matrix size and noise, we find that for SNR $\geq$ 10:1 the precision in area measurement is $<4\%$ for a sampling matrix of 256×256 ($\lambda = 4$, $\kappa \geq 4$) and $<2\%$ for a sampling matrix of 512×512 ($\lambda = 8$, $\kappa \geq 2$). These two scenarios are viable with the SNRs available from MRA techniques in use today.

REFERENCES

1. US. Department of Health and Human Services (DHHS). National Center for Health Statistics. Third National Health and Nutrition Examination Survey, 1999–1994. NHANES III Household Adult Data File (CD-ROM, Series 11, No. 1A). Hyattsville, MD.: Centers for Disease Control and Prevention, 1999.
2. Lin W, Haacke EM, Smith AS. Lumen definition in MR angiography. J Magn Reson Imaging 1991;1:327–336.
3. Gurleyik K, Haacke EM. Quantification of errors in volume measurements of the caudate nucleus using magnetic resonance imaging. J Magn Reson Imaging 2002;15:353–363.
4. Hoogeveen RM. Vessel visualization and quantification by magnetic resonance angiography. Ph.D. dissertation, Utrecht University, Utrecht, The Netherlands, 1998.
5. Chang YJ, Golby AJ, Albers GW. Detection of carotid stenosis from NASCET results to clinical practice. Stroke 1995;26:1325–1328.
6. de Koning PJH, Schaap JA, Janssen JP, Westenberg JJM, van der Geest RJ, Reiber JHC. Automated segmentation and analysis of vascular structures in magnetic resonance angiographic images. Magn Reson Med 2003;50:1189–1198.
7. Kozerke S, Botnar R, Oyre S, Scheidegger MB, Pedersen EM, Boesiger P. Automatic vessel segmentation using active contours in cine phase contrast flow measurements. J Magn Reson Imaging 1999;10:41–51.
8. Kim D, Park J. Computerized quantification of carotid artery stenosis using MRA axial images. Magn Reson Imaging 2004;22:353–359.
9. Hoogeveen RM, Bakker CJG, Viegerver MA. Limits to the accuracy of vessel diameter measurement in MR angiography. J Magn Reson Imaging 1998;8:1228–1235.
10. Lin W, Haacke EM, Smith AS, Clampitt ME. Gadolinium-enhanced high-resolution MR angiography with adaptive vessel tracking: preliminary results in the intracranial circulation. J Magn Reson Imaging 1992;2:277–284.

11. Lin W, Haacke EM, Masaryk TJ, Smith AS. Automated local maximum-intensity projection with three-dimensional vessel tracking. J Magn Reson Imaging 1992;2:519–526.
12. Westenberg JJM, van der Geest RJ, Wasser MNJM, et al. Vessel diameter measurements in gadolinium contrast-enhanced three-dimensional MRA of peripheral arteries. Magn Reson Imaging 2000;18:13–22.
13. Parker DL, Chapman BE, Roberts JA, Alexander AL, Tsuruda JS. Enhanced image detail using continuity in the MIP Z-buffer: applications to magnetic resonance angiography. J Magn Reson Imaging 2000;11:378–388.
14. Hänni M, Edvardsson H, Wågberg M, Pettersson K, Smedlby Ö. Quantification of atherosclerosis with MRI and imaging processing in spontaneously hyperlipidemic rabbits. J Cardiovasc Magn Reson 2004;6:675–684.
15. Thomas JB, Rutt BK, Ladak HM, Steinman DA. Effect of black blood MR image quality on vessel wall segmentation. Magn Reson Med 2001;46:299–304.
16. Yuan C, Lin E, Millard J, Hwang J. Closed contour edge detection of blood vessel lumen and outer wall boundaries in black-blood MR images. Magn Reson Imaging 1999;17:257–266.
17. Zhang S, Cai J, Luo Y, et al. Measurement of carotid wall volume and maximum area with contrast-enhanced 3D MR imaging: initial observations. Radiology 2003;228:200–205.
18. Chapman BE, Goodrich KC, Alexander AL, Blatter DD, Parker DL. Evaluation of measures of technical image quality for intracranial magnetic resonance angiography. Comput Biomed Res 1999;32: 530–556.
19. Kong W, Haacke EM. Estimation of cross sectional accuracy as a function of resolution, signal-to-noise and vessel diameter. In: Proceedings of the 8th Annual Meeting of ISMRM, Denver, CO, USA, 2000 (Abstract 693).
20. Scheid FJ. Schaum's outline of theory and problems of numerical analysis. New York: McGraw Hill; 1989. 471 p.
21. Du YP, Parker DL, Davis WL, Cao G. Reduction of partial-volume artifacts with zero-filled interpolation in three-dimensional MR angiography. J Magn Reson Imaging 1994;4:733–741.
22. Haacke EM, Brown RW, Thompson MR, Venkatesan R. Signal, contrast and noise. In: Magnetic resonance imaging: physical principles and sequence design. New York: John Wiley and Sons; 1999. 914 p.
23. Bernstein MA, Fain SB, Riederer SJ. Effect of windowing and zero-filled reconstruction of MRI data on spatial resolution and acquisition strategy. J Magn Reson Imaging 2001;14:270–280.
24. Venkatesan R, Haacke EM. Role of high resolution in magnetic resonance (MR) imaging: applications to MR angiography, intracranial T1-weighted imaging, and image interpolation. Int J Imaging Syst Technol 1997;8:529–543.
25. Venkatesan R. Improvement of object visibility in high-resolution magnetic resonance imaging. Masters thesis, Case Western Reserve University, Cleveland, OH, 1994.
26. Thunberg P, Karlsson M, Wigström L. Accuracy and reproducibility in phase contrast imaging using SENSE. Magn Reson Med 2003; 50:1061–1068.